Journal of Computational Physics 228 (2009) 3189–3208

Contents lists available at ScienceDirect

Journal of Computational Physics

journal homepage: www.elsevier.com/locate/jcp

DNS of buoyancy-dominated turbulent flows on a bluff body using the immersed boundary method

Seongwon Kang *, Gianluca Iaccarino, Frank Ham

Center for Turbulence Research, Stanford University, 488 Escondido Mall, Building 500, Room 501N3, Stanford, CA 94305, USA

ARTICLE INFO

Article history:
Received 25 August 2008
Received in revised form 5 December 2008
Accepted 10 December 2008
Available online 16 January 2009

Keywords:
Immersed boundary
Conjugate heat transfer
Turbulent flow
Bluff body
Buoyancy

ABSTRACT

A novel immersed boundary (IB) method has been developed for simulating multi-material heat transfer problem – a cylinder in a channel heated from below with mixed convection. The method is based on a second-order velocity/scalar reconstruction near the IB. A novel algorithm has been developed for the IB method to handle conjugate heat transfer. The fluid–solid interface is constructed as a collection of disjoint faces of control volumes associated to different material zones. Coupling conditions for the material zones have been developed such that continuity and conservation of the scalar flux are satisfied by a second-order interpolation. Predictions of the local Nusselt number on the cylinder surface show good agreement with the experimental data. The effect of the Boussinesq approximation on this problem was also investigated. Comparison with the variable density formulation suggests that, in spite of a small thermal expansion coefficient of water, the variable density formulation in a transitional flow with mixed convection is preferable.

1. Introduction

The immersed boundary (IB) method is a numerical technique to enforce boundary conditions on surfaces not aligned with the mesh. This method has become popular for flow problems involving very complex geometries often encountered in engineering applications. Compared to a body-fitted mesh, the IB method is advantageous in three situations. First, it provides an alternative to body-fitted mesh for very complex geometry; in this case, the amount of user interventions and turn-around time for mesh generation can be reduced by using a simpler mesh structure. The second advantage relates to problems associated with moving geometries. Since the effect of geometry is imposed in the solution step, it is relatively straightforward to include boundary motion and possible interactions between fluid flow and structures. Another advantage presents itself in multi-phase or multi-material problems. More specifically, the interface between different materials can be regarded as an immersed boundary. The IB method is then equivalent to the imposition of physical conditions at the interface.

The IB method was first introduced by Peskin [28] for computing blood flow in the cardiovascular system. Subsequently, there have been numerous efforts to enhance the accuracy, stability and range of applicability of the IB method. Readers can refer to articles by [24,15] for information on the previous studies. So far, IB methods have been applied to a wide range of applications: compressible flows [7,22], particulate flows [36,38], micro-scale flows [1], interaction with solid bodies ([8,40], among others), multi-phase flows [6], conjugate heat transfer [14,39], environmental flows [33], bio-fluids [5], etc. However, the number of published studies which validated near-wall statistics of turbulent flows is relatively small.

* Corresponding author.
E-mail address: seongwon@stanford.edu (S. Kang).

0021-9991/$ - see front matter © 2008 Elsevier Inc. All rights reserved.
doi:10.1016/j.jcp.2008.12.037

In the present study, we explore a turbulent conjugate heat transfer problem where the modes of convective and conductive heat transfer are handled simultaneously. Problems with conjugate heat transfer are very common in industrial applications, thus may benefit greatly from easier mesh generation accomplished by the IB method.

In the literature, conjugate heat transfer in turbulent flows has been widely investigated. The majority of the studies have used RANS-based models ([37,26,13,12], among others). Very few studies have used LES or DNS for conjugate heat transfer problems. Tiselj et al. [35] applied DNS to a conjugate heat transfer between a turbulent channel flow and a solid wall. This study yielded improved results compared to those obtained with RANS. Smirnova and Kalaev [32] applied a LES approach to a problem of crystal growth. Both studies used a body-fitted methods. Iaccarino and Moreau [14] applied the IB method to conjugate heat transfer problems using a RANS model. Yu et al. [39] applied a distributed Lagrange multiplier-based fictitious domain method to a conjugate heat transfer problem of a particulate flow at low Reynolds number. Song et al. [34] used an IB method to investigate the effect of thermal resistance of solid wall on turbulent heat transfer in a ribbed channel. Certainly, there are very few previous studies that have used an IB method for LES/DNS of a conjugate heat transfer problem.

The objective of the present study is to assess the accuracy and efficiency of the IB method for LES/DNS of a turbulent conjugate heat transfer problem. For this purpose, a novel method is developed by extending an existing IB method to multi-material problems and verified using a simple analytic solution. The present validation study is focused on a mixed, conjugate, transitional heat transfer problem around a heated cylinder in a channel heated from below [21]; we compare the present computation to the experiment for the near-wall temperature field, the transition to turbulence due to thermal instabilities, and the validity of the Boussinesq approximation.

In the next section, description of numerical schemes – the flow solver, the IB method and extension to multi-material problems – are presented. Section 3 shows a verification study to test accuracy of the developed IB method. Results from simulations of a heated cylinder are presented in Section 4. From parametric studies on flow and computational conditions, conclusions are derived in Section 5.

2. Numerical methods

2.1. Description of the Navier–Stokes solvers

In the present study, a heat transfer problem with mixed convection is considered. The variable density formulation of the Navier–Stokes equations is written as:

$$\frac{\partial \rho u_i}{\partial t}+\frac{\partial \rho u_i u_j}{\partial x_j}=-\frac{\partial p}{\partial x_i}+\frac{\partial}{\partial x_j}\left[\mu\left(\frac{\partial u_i}{\partial x_j}+\frac{\partial u_j}{\partial x_i}\right)\right]+\rho g_i, \tag{1}$$

$$\frac{\partial \rho}{\partial t}+\frac{\partial \rho u_i}{\partial x_i}=0, \tag{2}$$

$$\frac{\partial \rho h}{\partial t}+\frac{\partial \rho u_j h}{\partial x_j}=\frac{\partial}{\partial x_j}\left[k\frac{\partial T}{\partial x_j}\right], \tag{3}$$

where t is the time, ρ is the density, u_i is the velocity, p is the pressure, μ is the molecular viscosity, and g_i is the vector of the gravitational acceleration. T is the temperature, $h = c_pT$ is the enthalpy, and k is the thermal conductivity. Note that ρ,μ and k are functions of the temperature for water [19].

The solution of the Navier–Stokes equations (1)–(3) is obtained using a solver called CDP[1]: a fully implicit LES solver based on an unstructured collocated mesh. In this code, the time-staggered scheme of [29] is employed. Then, the discretized momentum equation at $(n + 1/2)$th time step is written as:

$$\frac{\rho^{n+1}u_i^{n+1}-\rho^n u_i^n}{\Delta t}+\frac{1}{2}\frac{\partial\left[(\rho u_j)^{n+\frac{1}{2}}(u_i^{n+1}+u_i^n)\right]}{\partial x_j}=-\frac{\partial p^{n+\frac{1}{2}}}{\partial x_i}+\frac{1}{2}\frac{\partial}{\partial x_j}\left[\mu\left(\frac{\partial u_i}{\partial x_j}+\frac{\partial u_j}{\partial x_i}\right)^{n+1}+\mu\left(\frac{\partial u_i}{\partial x_j}+\frac{\partial u_j}{\partial x_i}\right)^{n}\right]+\frac{1}{2}(\rho^{n+1}+\rho^n)g_i, \tag{4}$$

and the discretized continuity and energy equations at n-th time step are:

$$\frac{\rho^{n+\frac{3}{2}}-\rho^{n+\frac{1}{2}}}{\Delta t}+\frac{\partial \rho^{n+1}u_i^{n+1}}{\partial x_i}=0, \tag{5}$$

$$\frac{\rho^{n+\frac{3}{2}}h^{n+\frac{3}{2}}-\rho^{n+\frac{1}{2}}h^{n+\frac{1}{2}}}{\Delta t}+\frac{1}{2}\frac{\partial\left[(\rho u_j)^{n+1}\left(h^{n+\frac{3}{2}}+h^{n+\frac{1}{2}}\right)\right]}{\partial x_j}=\frac{1}{2}\frac{\partial}{\partial x_j}\left[k\frac{\partial T^{n+\frac{3}{2}}}{\partial x_j}+k\frac{\partial T^{n+\frac{1}{2}}}{\partial x_j}\right], \tag{6}$$

where Δt is the time step. In CDP, the spatial derivatives are computed using a finite volume method (FVM) for node-based collocated mesh. The flux at the face of a control volume is evaluated by applying a second-order interpolation and mid-point

[1] CDP is named after Charles David Pierce (1969–2002).

rule for numerical integration. Further details about CDP are available in [10,9]. To solve the discretized equations (Eqs. (4)–(6)) efficiently, a variant of the fractional-step method [20] is employed.

In order to achieve optimal control of the grid size, locally refined meshes (i.e., a mesh consisting of hexahedral elements with hanging nodes) are used with the IB method. Several approaches have been used in the previous studies for the treatment of hanging nodes ([31,11,3,25], among others). In the present study, elements around hanging nodes are treated as unstructured polyhedral control volumes. It is obviously more time-consuming to use a solver for unstructured meshes with the IB method than to use a solver specifically developed for structured meshes. However, locally refined meshes can be treated without modifications in the present framework; moreover, it can easily support load-balanced computations in a massively parallel computing environment. Further details on local mesh refinement in the present study are available in [18].

In addition to the variable density formulation, we considered the incompressible Navier–Stokes equations with the Boussinesq approximation and constant material properties:

$$\frac{\partial u_i}{\partial t}+\frac{\partial u_i u_j}{\partial x_j}=-\frac{1}{\rho}\frac{\partial p}{\partial x_i}+\nu\frac{\partial^2 u_i}{\partial x_j \partial x_j}-g_i\beta(T-T_\infty), \tag{7}$$

$$\frac{\partial u_i}{\partial x_i}=0, \tag{8}$$

$$\frac{\partial T}{\partial t}+\frac{\partial T}{\partial x_j}=\alpha\frac{\partial^2 T}{\partial x_j \partial x_j}, \tag{9}$$

where ν is the kinematic viscosity, α is the thermal diffusivity, β is the coefficient of thermal expansion, and T_∞ is the far-field temperature. This problem is dependent on three non-dimensional parameters – the Reynolds number ($Re = U_0 L/\nu$), the Grashof number ($Gr = g\beta\Delta T L^3/\nu^2$), and the Prandtl number ($Pr = \nu/\alpha$). U_0 is a reference velocity, L is a reference length, and ΔT is a reference temperature difference.

2.2. Description of the immersed boundary-approximated domain method (IB-ADM)

The present IB method for conjugate heat transfer is based on an IB method called the immersed boundary-approximated domain method (IB-ADM). This method is discussed in detail in [18] and only briefly described in this section.

The IB-ADM is based on the interpolation method of [4] which employs reconstruction of the velocity and scalar near the IB. However, IB-ADM augments the original method by satisfying an additional constraint on the pressure which decouples the flow domain from other physically unrelated domains. This guarantees the pressure accuracy and enables the method to handle very thin solid interfaces accurately. Fig. 1 shows an example of the immersed boundary (thick black line, Γ_{IB}), the approximated domain (shaded area, Ω_a), and approximated boundary (thick gray line, Γ_a). The Ω_a is identified by excluding the grid cells crossed by the IB from the fluid region Ω_{fluid}. In IB-ADM, the discretized governing equations are satisfied without modification inside Ω_a, and the reconstruction method is used only to provide the velocity/scalar boundary conditions of Ω_a. Fig. 2 shows the reconstructed velocity components on Γ_a for the staggered, CV-collocated and node-collocated arrangements of the velocity variables. This leads to an additional condition for global mass conservation:

$$\int_{\Gamma_a}\rho\vec{u}\cdot d\vec{A}=\int_{\Gamma_{IB}}\rho\vec{u}\cdot d\vec{A}, \tag{10}$$

which is satisfied by a least-square algorithm.

Specifically, consider an interpolation method for the velocity:

$$\vec{u}_m=\sum_{nb}w_{nb,m}\vec{u}_{nb,m}+w_{IB,m}\vec{u}_{IB,m}, \tag{11}$$

where m is the index of the face in Γ_a where $\vec{u}_m$ is located, $w_{nb,m}$ is the interpolation coefficient, nb denotes the index of neighboring points, $\vec{u}_{nb,m}$ is the neighboring velocity of $\vec{u}_m$, and $\vec{u}_{IB,m}$ is the velocity at an IB position that is the boundary-normal projection of the point of $\vec{u}_m$. Eq. (11) is second-order accurate but does not necessarily satisfy mass conservation [18]. The constraint of global mass conservation Eq. (10) is satisfied by a correction term:

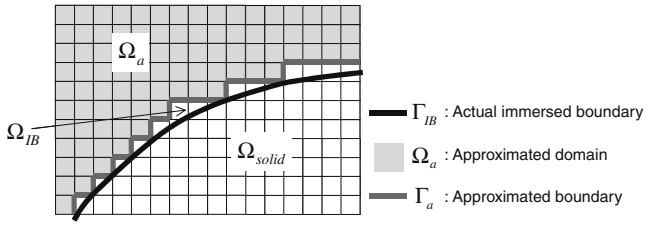

Fig. 1. Examples of the approximated domain and boundary.

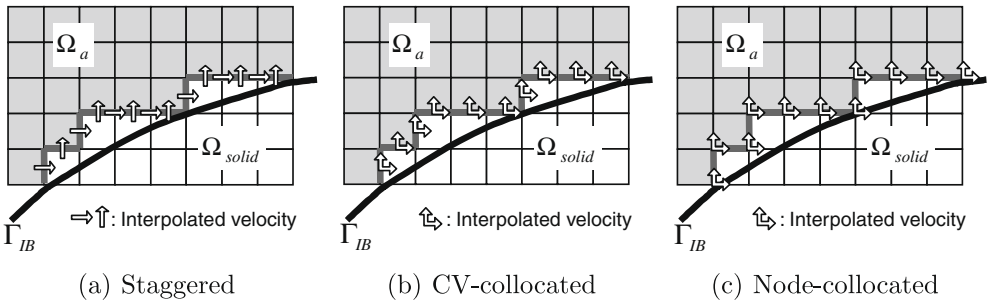

Fig. 2. Examples of the interpolated velocity components on the approximated boundary Γ_a in different arrangements of the velocity variables.

$$\vec{u}_m = \sum_{nb} w_{nb,m}\vec{u}_{nb,m} + w_{IB,m}\vec{u}_{IB,m} + \frac{Q_e}{\rho_m}\frac{\sum_k x_{k,m}^2}{\sum_m^{N_a}\sum_k x_{k,m}^2|\vec{A}_m|^2}\vec{A}_m, \tag{12}$$

where Q_e is the error of Eq. (11) to the mass constraint, N_a denotes the total number of the faces in Γ_a, $\sum_k$ is summation over $k = 1-3$, $\vec{A}_m$ is the outward-normal face-area vector at the face, $x_{k,m}$ is the relative location of $\vec{u}_m$ to the $\vec{u}_{IB,m}$, and ρ_m is the density at this location.

In the present approach, imposing boundary conditions at Γ_a results in all flow variables (velocity, pressure and scalar) at CVs in Ω_{solid} and CVs crossed by the IB being excluded from the computation. This, therefore, does not cause an unrealistic flow in the solid region. In numerical tests, IB-ADM showed second-order accuracy for velocity, pressure and scalar fields, and was validated with DNS of a turbulent channel flow and LES of a flow around an airfoil at $Re_c = 150{,}000$ (c is the chord length) to correctly predict the statistics of wall flow variables. Detailed results are available in [18].

2.3. Implementation for a multi-material problem (conjugate heat transfer)

In the previous section, the description of the present IB method focused exclusively on a single fluid region. This approach can be extended easily to problems with multiple materials with different properties. An example of multi-material problems is a conjugate heat transfer problem where convective heat transfer in the fluid and conductive heat transfer in the solid are handled simultaneously. The IB method was first applied to conjugate heat transfer problems in [14,39]. A problem with the turbulent conjugate heat transfer will be presented in Section 4.

As previously noted, in the IB-ADM framework, different domains (fluid and solid) across the IB are completely segregated in the discretized governing equations. In several existing numerical methods for multi-phase or multi-material problems, the discretization stencil for governing equations are maintained at the phase (material) interface. This can simplify the implementation but tends to increase the numerical stiffness when the ratio of material properties across the interface is very large. In the present approach, approximated boundaries are created and therefore a one-sided boundary discretization is used. Our approach is notionally similar to sub-domain methods for multi-block grids with discontinuous grid interface in the sense that the boundary conditions are communicated across the interface iteratively in the matrix solution step.

Fig. 3 shows the three steps necessary to build the communication across the interface between two adjoining materials. Starting from the true fluid–solid interface, two approximated boundaries facing each other across the true interface (Γ_{fluid} and Γ_{solid} in Fig. 3(b)) are constructed. The approximated boundaries are built as in the previous section. The final stage is to build connections between points on the two approximated boundaries. If these are projected onto the true material interface, then these projected boundaries can be considered as two adjoining discontinuous grids. Fig. 3(c) shows a simplified two-dimensional example. Interpolation on this surface is used to communicate information across the interface. To summarize, the present study takes the following four steps to build the interpolation coefficients:

(1) Locate the wall-normal projection onto the true material interface for the two approximated boundaries.
(2) For each data point of one projected boundary (i.e., zone A), find a triangle in the other projected boundary (zone B) so that the area of the triangle is smallest among those that encompass the data point in zone A.
(3) Build interpolation coefficients from the three points in zone B to the data point in zone A using a second-order polynomial.
(4) Repeat steps (2)–(3) in order to build interpolation coefficients for data points in zone B.

Fig. 4 presents the steps (2)–(3) in an example. For a data point in projected zone A (P_A, gray), an encompassing triangle (shaded one) of points in projected zone B is found. Here, $P_{B,c} = (P_{B,1} + P_{B,2} + P_{B,3} + P_{B,4})/4$. Then, the interpolation for P_A is constructed using $P_{B,1}$,$P_{B,2}$ and $P_{B,c}$ using a linear polynomial. In practice, P_A may not be in the plane of ($P_{B,1}$,$P_{B,2}$,$P_{B,c}$). Thus, the normal projection of P_A is used instead.

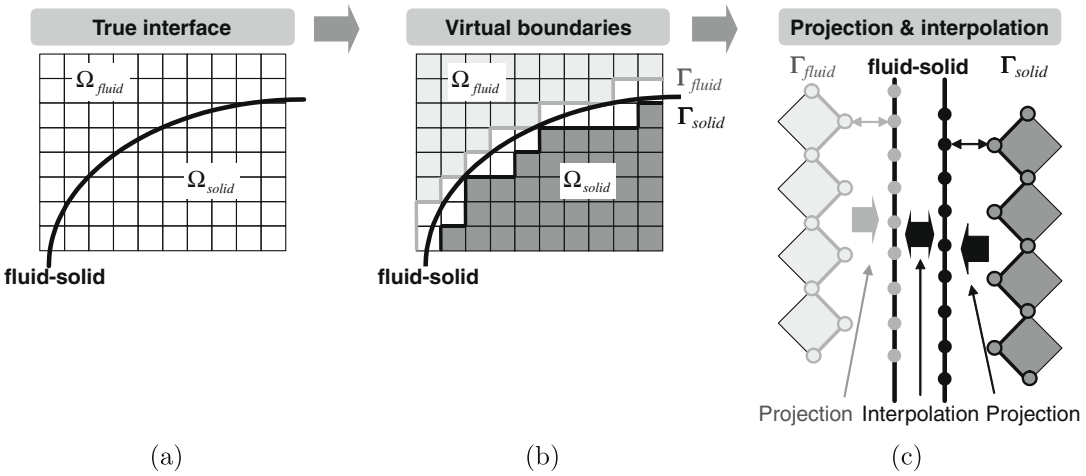

Fig. 3. Schematic diagrams for interface treatment between different materials: (a) true fluid–solid interface; (b) construction of approximated boundaries facing each other (Γ_{fluid} and Γ_{solid}); (c) computation of interpolation coefficients from the projected boundaries.

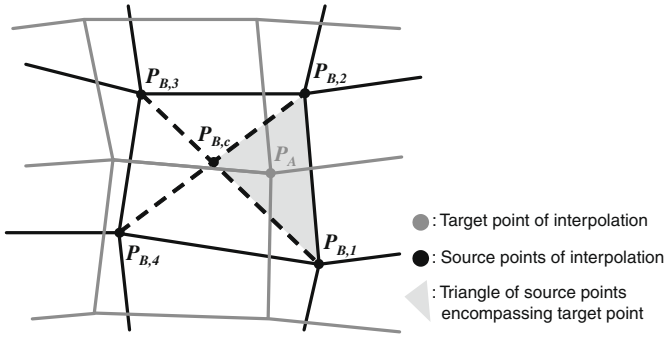

Fig. 4. Schematic diagram for finding interpolation coefficients from zone B to A.

This initialization is a general process for building connection between approximated boundaries; it is not specific to conjugate heat transfer problems. However, the data communicated across the material interface are specific to a given problem. Here, continuity of the temperature field and balance of the heat flux must be satisfied at the interface:

$$T_{fluid} = T_{solid}, \tag{13}$$

$$k_{fluid}\frac{\partial T}{\partial \mathbf{n}}\bigg|_{fluid} = k_{solid}\frac{\partial T}{\partial \mathbf{n}}\bigg|_{solid}, \tag{14}$$

where $\mathbf{n}$ denotes the normal to the true interface and k denotes the thermal conductivity of a material.

In the present method, these conditions are adapted as boundary conditions. Because it is impossible to use both conditions as boundary conditions for single domain, Eqs. (13) and (14) are asymmetrically satisfied at the approximated boundaries of fluid and solid domains. Specifically, the Dirichlet B.C. (Eq. (13)) is enforced at the boundary of the fluid domain, while the Neumann B.C. (Eq. (14)) is enforced at the boundary of the solid domain. These are the modified boundary conditions for each domain:

$$T_{fluid} = \widehat{T_{solid}}, \tag{15}$$

$$k_{solid}\frac{\partial T}{\partial \mathbf{n}}\bigg|_{solid} = k_{fluid}\widehat{\frac{\partial T}{\partial \mathbf{n}}\bigg|_{fluid}}, \tag{16}$$

where $\widehat{\ }$ denotes interpolation from the source to the target boundary. The wall-normal heat flux is computed from the reconstruction formula for imposing the boundary conditions, which is equivalent to one-side finite difference.

In the matrix solution step, the boundary conditions are interpolated and communicated across the interface. This update process is performed during every iteration of the solution step, until the residual is smaller than a preset convergence criterion. The Dirichlet B.C. is chosen for the fluid domain because it is naturally more stable than the Neumann B.C. and the heat conductivity of the solid is typically much greater than the fluid.

The present method is based on a second-order interpolation method; therefore, the communication process and asymmetric way of satisfying the energy equation at the material interface (i.e., Eqs. (15) and (16)) have second-order accuracy. However, a first-order error term is generated during the process of computing the heat flux at the interface because one-side finite difference is used for the first-order derivative. A first-order error term is also generated in imposition of the Neumann B.C. (Eq. (16)). As a result, the accuracy of overall method is reduced to first order. Increasing the accuracy is possible by increasing the width of discretization stencil and using a higher-order reconstruction formula (e.g. quadratic interpolation), but this was not pursued in the present study, because very fine grids are used and the results are not too sensitive to the accuracy close to the wall.

3. Verification study

3.1. Flow around a heated sphere

A steady flow around a heated sphere was computed to validate the IB method in a heat transfer problem. When a sphere positioned in a quiescent fluid is heated to a temperature higher than the ambient, the density gradient in the fluid drives the flow upward (natural convection). The local Nusselt number on the sphere surface is compared to results from simulations with a body-fitted mesh.

The Grashof number (Gr) based on the radius (R) of the sphere is 10^4, the Reynolds number is $Re = Gr^{0.5}$, and the Prandtl number is $Pr = 0.72$. Fig. 5 shows the computational mesh of the present study. Again, the mesh is generated by means of the refinement algorithms introduced before. The far-field boundary is located at $r = 16R$, where r is the distance from the center of the sphere. A non-dimensional temperature $\Theta = (T - T_f)/(T_s - T_f)$ is introduced where T_s and T_f are the sphere and far-field temperatures, respectively. Θ is then set to 1 at the sphere and 0 at the far-field boundary. For the velocity, the no-slip condition is enforced at the sphere and far-field boundary. The total number of grid points is 2.0 million. The grid spacing near the sphere is about $0.01R$. For the body-fitted simulations, the same flow solver and structured meshes in spherical coordinates are used. The grid spacing in every coordinate is 1/2 (coarse mesh) or 1/4 (fine mesh) of the mesh used in [17]. The coarse mesh has a resolution near the sphere similar to the mesh in Fig. 5.

Fig. 6(a) shows contours of the streamwise (y) velocity and temperature. A steady flow is obtained at this Grashof number. Fig. 6(b) shows the non-dimensionalized heat transfer coefficient compared to simulations using a body-fitted mesh. Agreement between the present IB and body-fitted simulations is satisfactory. Difference between the body-fitted simulations is less than 0.5% which shows grid convergence.

Jia and Gogos [17] mentioned a few correlations between the averaged Nusselt number and non-dimensional parameters proposed by previous studies based on experiments and theory for natural convection around a sphere. In Table 1, our result agrees reasonably well with each other and [17].

Table 1
Averaged Nusselt number at the wall compared to previous studies.

	Body-fitted (coarse)	IB	[17]	[23]	[2]
$\bar{N}u = 2\bar{h}R/k$	8.63	8.60	8.74	9.75	9.05

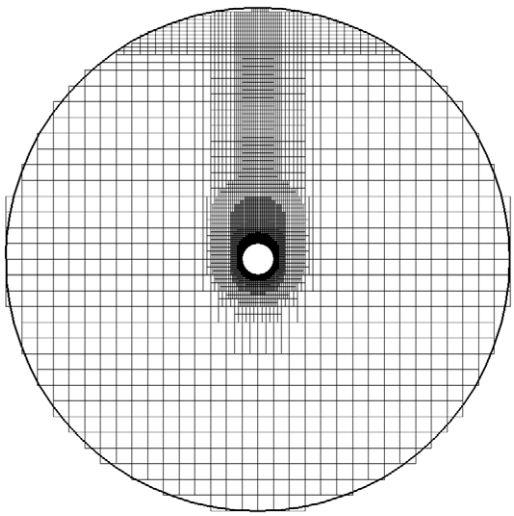

Fig. 5. Locally refined mesh for a heated sphere.

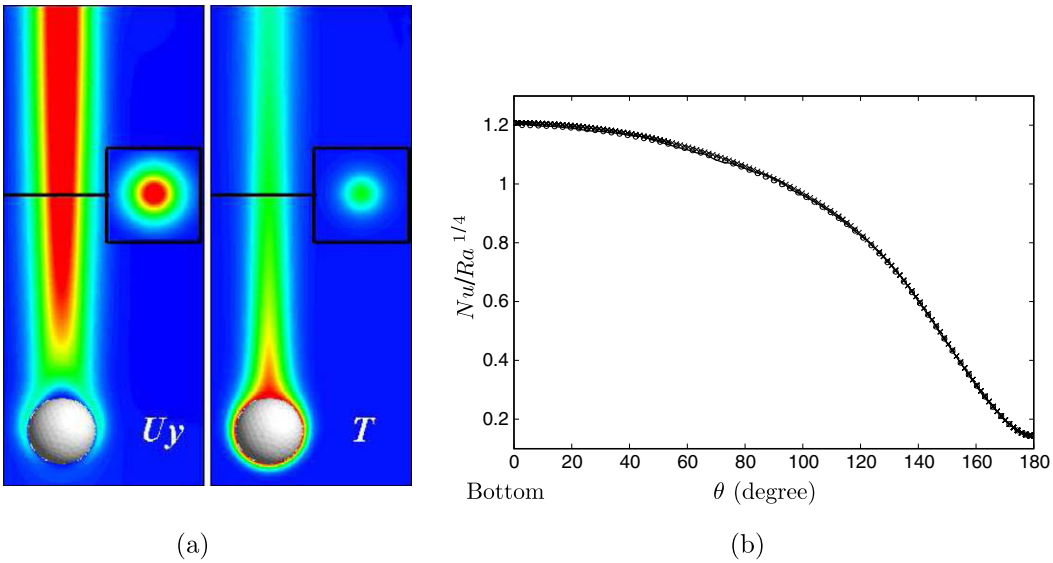

Fig. 6. Results of the case with $Gr = 10^4$: (a) contours of the y-velocity and temperature; (b) heat transfer coefficients. ⊙, body-fitted simulation (coarse); ×, body-fitted simulation (fine); —, IB simulation.

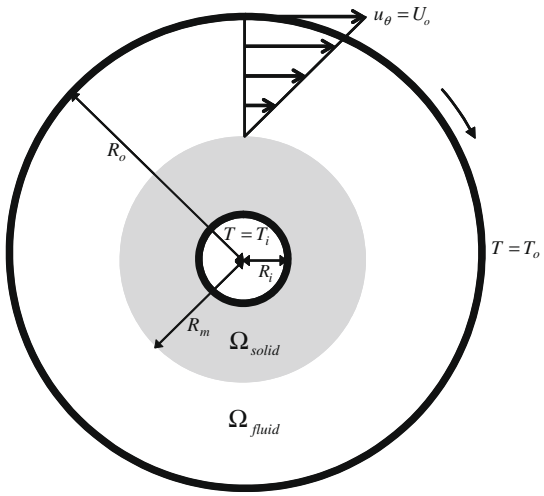

Fig. 7. A conjugate heat transfer problem of a rotating flow between two coannular cylinders. Thick lines denote boundaries where temperature boundary condition is imposed.

3.2. Accuracy of the IB method for conjugate heat transfer

The accuracy of the method in Section 2.3 was verified with a two-dimensional laminar test case. Fig. 7 shows a schematic diagram of a heat transfer problem between two coannular cylinders. A fluid is rotating between the inner and outer cylinders. The outer cylinder is rotating so that the radial velocity at the wall is U_o, while the inner cylinder is stationary. The temperature is set to T_i at the inner wall of the inner cylinder and T_o at the wall of the outer cylinder. The energy balance Eqs. (15) and (16) are satisfied at the interface ($r = R_m$) between the fluid and inner cylinder. The radius of the inner and outer walls of the inner cylinder and the wall of the outer cylinder is $R_i = 0.45$,$R_m = 0.9$and $R_o = 1.8$, respectively. The ratio of constant heat conductivities between the solid and fluid (k_s/k_f) is set to 9. This problem has an analytic solution that satisfies two-dimensional steady Navier–Stokes and energy equations with energy balance at the interface, Eqs. (13) and (14):

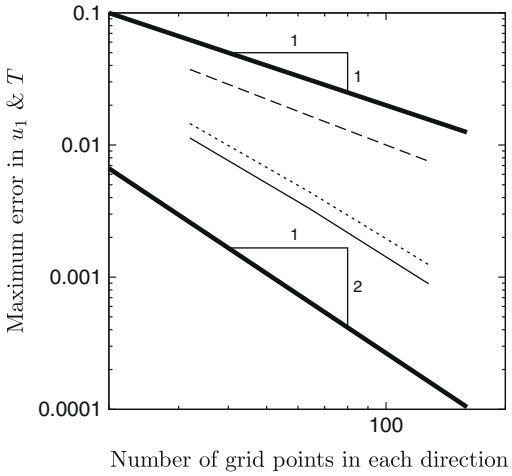

Fig. 8. Maximum errors in the velocity and temperature for the conjugate heat transfer problem between two coannular cylinders: —, x-velocity; - - - -, temperature; ····, temperature with the exact temperature at $r = R_m$.

$$u_\theta = 0, \quad u_r(r) = \begin{cases} 0 & \text{for } R_i < r < R_m \text{ (solid)}, \\ -\frac{R_o R_m^2 U_o}{R_o^2 - R_m^2}\frac{1}{r} + \frac{R_o U_o}{R_o^2 - R_m^2} r & \text{for } R_m < r < R_o \text{ (fluid)}, \end{cases} \tag{17}$$

$$T(r) = \begin{cases} T_i + \frac{T_o - T_i}{\log(R_m/R_i) + (k_s/k_f)\log(R_o/R_m)} \log\left(\frac{r}{R_i}\right) & \text{for } R_i < r < R_m, \\ T_o - \frac{T_o - T_i}{(k_f/k_s)\log(R_m/R_i) + \log(R_o/R_m)} \log\left(\frac{R_o}{r}\right) & \text{for } R_m < r < R_o, \end{cases} \tag{18}$$

where r and θ denote the radial and azimuthal directions. Steady velocity and temperature fields were computed for three different grid spacings. The accuracy was then deduced by comparing the maximum error versus the grid spacing. Fig. 8 shows the maximum error in the velocity and temperature. The temperature shows an accuracy less than second order, but higher than first order (=1.5). As mentioned in Section 2.3, this is due to the limited width of discretization and reconstruction stencils for the Neumann B.C. The velocity is second-order accurate because of the Dirichlet B.C. at both walls. When the exact temperature at $r = R_m$ is imposed as the Dirichlet B.C. (the dotted line), the temperature shows second-order accuracy.

4. A heated cylinder in a channel heated from below

In this section, the IB method is applied to a turbulent conjugate heat transfer problem investigated both experimentally and numerically by Laskowski et al. [21]. This problem involves mixed convection, transition to turbulence, and conjugate heat transfer. The most important metric for validation is the time-averaged heat flux at the interface between the fluid and the solid.

4.1. Experimental configuration

Fig. 9 shows the configuration used in [21], based on water flow in a channel. The bottom wall is heated to a high temperature from the streamwise (x) location $x = 0$. This surface heating results in a thermal boundary layer developing along the bottom wall. A horizontal tube made of stainless steel is placed along the spanwise (z) direction. The wall-normal (y) location of the tube is approximately the edge of the mean thermal boundary layer. The outer and the inner walls of the tube are referred to as the outer and the inner cylinder, respectively. Inside the inner cylinder, there is a flow of hot water that heats the tube. The thermal boundary layer developing along the bottom wall interacts with the heat flux transferred from

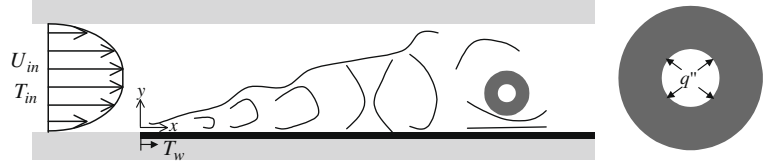

Fig. 9. Schematic diagram of a heated cylinder inside a channel heated from below.

the inner cylinder to the outer cylinder. The Reynolds number, based on the mean streamwise velocity (U_{in}) and the channel half-width ($H/2$), is approximately 414, which would result in laminar flow in isothermal conditions. However, thermal plumes generated by the buoyancy force triggers transition to turbulence.

The length (L) and height (H) of the test section in the experiment are 61 cm and 7.62 cm, respectively. The spanwise domain size is 61 cm. The mean streamwise velocity (U_{in}) and temperature (T_{in}) of the inflow approaching the test section are 1.09 cm/s and 284 K, respectively. For $x = 0$–61 cm, the temperature at the bottom wall (T_w) is 318 K, while the top wall is adiabatic. The streamwise and wall-normal location of the center of the tube is $(x_{cyl}, y_{cyl}) = (42.7\text{ cm}, 1.43\text{ cm})$. The diameters of the inner (d_i) and outer cylinder (d_o) are 6.35 mm and 15.875 mm, respectively. The temperature and mass flux of the water flow inside the inner cylinder are not documented in [21], nor is the heat flux from the inner cylinder. The temporally and spatially averaged temperature (T_{cyl}) at the outer cylinder is 311.3 K.

The statistical data on the temperature field available in [21] are the time-averaged temperature and heat flux at the outer cylinder, for both the experiment and their RANS computations. The time-averaged streamwise velocity and kinetic energy profiles are also available for both cases at $x = 0$ and 5 cm upstream of the cylinder. These are used as the validation data in the present study.

4.2. Computational setup

The computational conditions used in the present study are the same as in the experiment, with a few modifications to the boundary conditions and the domain size.

With regard to the inlet velocity, [21] indicated that it is a laminar flow. The time-averaged streamwise velocity profile at $x = 0$ without heating from below is available in [21]. In the preliminary study, a uniform flow starting at $x = -50$ cm was used in order to create a velocity profile at $x = 0$ in agreement with the experiment. With heating from below, the values of the RMS velocity as well as the temperature are virtually zero before $x = -2$ cm. Based on this result, the streamwise domain size is selected as $-3\text{ cm} < x < 61$ cm. A few different inlet velocity B.C.s are tested, including an interpolated velocity profile from the experiment. This velocity B.C. is steady in time, even though unsteady effects might be present in the experiment. T_{in} is used as the Dirichlet B.C. at the inlet.

The domain size in the spanwise direction is reduced to 15 cm to limit the simulation cost. Based on the analysis of the present instantaneous flow fields, we concluded that this spanwise size is sufficient. The size of a thermal plume initially generated near $x = 0$ due to the Rayleigh–Taylor instability (i.e., the size of the smallest coherent structure) is observed to be less than 1.3 cm in the spanwise direction.

The velocity B.C. at the walls is the no-slip condition. At the outlet at $x = 61$ cm, the convective outflow condition [27] is used for both velocity and temperature. The temperature B.C.s at the bottom and top walls are the same as in the experiment. Since the heat flux at the inner cylinder was not measured, we assume it was constant. The value of the constant heat flux is adjusted during the simulation such that the measured averaged temperature at the outer cylinder matches the value

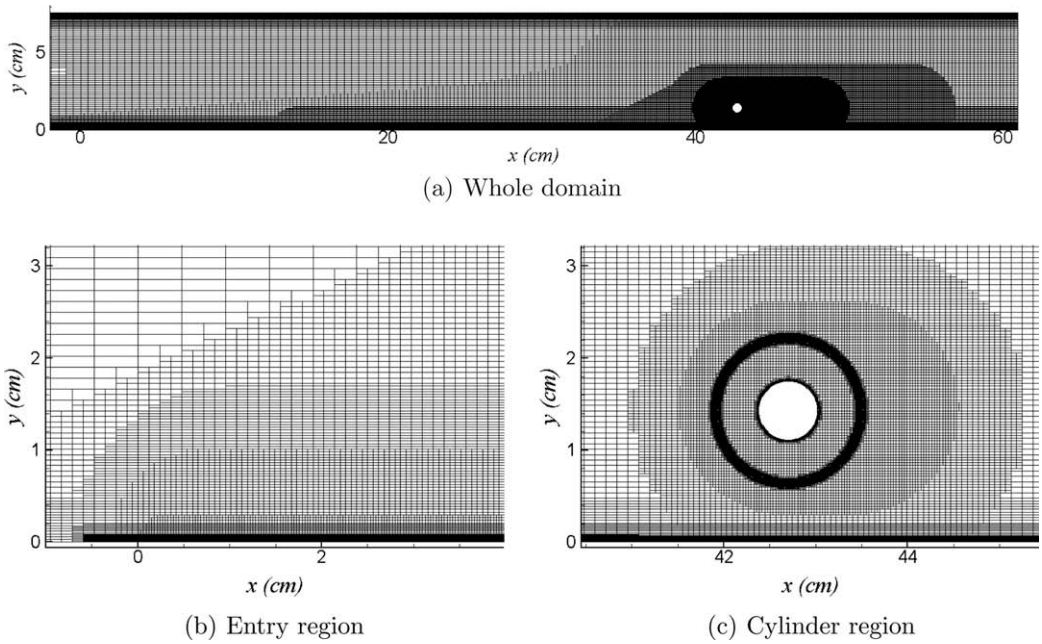

Fig. 10. The locally refined mesh for the heated cylinder case.

(T_{cyl}) from the experiment. After a simulation, the value of the constant heat flux is updated to compensate for the difference in T_{cyl} between the simulation and experiment. This process is iterated until the difference in T_{cyl} is less than 0.2°; this typically increased the cost of the computation by a factor of at least three.

Eqs. (1) and (3) are used as the governing equations. Material properties – the viscosity (μ), density (ρ), thermal conductivity (k), and specific heat at constant pressure (c_p) – are functions of the temperature. For water, the tabulated data from [19] are used. For the stainless steel cylinder, the data for AISI-304 from [16] are used. The specific type of stainless steel is not described in [21]. For the gravitational acceleration, we set g_i, $(g_x, g_y, g_z) = (0, -981\ \mathrm{cm/s^2}, 0)$.

Fig. 10 shows an example of the locally refined mesh used in the present study. Several grids consisting of 6–12 million points were tested in order to assess the resolution requirement. Details of the grid study are presented in the next section. A broad spectrum in the geometric scales exists in the present problem. More specifically, the channel length is 61 cm, while the radius of the outer cylinder is 0.79 cm. We found that the local mesh refinement technique is very useful to reduce the number of mesh points, since it can achieve a rapid spatial change in the mesh resolution. The computational time step Δt is chosen so that the maximum CFL number is 1.9. The region of a high CFL number is very localized near the cylinder where the mesh spacing is smallest.

4.3. Effect of grid resolution

Because the present problem involves transition to turbulence, it is expected to be very sensitive to flow and computational conditions; in particular, the mesh resolution is especially important.

Three different mesh resolutions were tested in the present study. We observed that the region most sensitive to the mesh resolution is near the bottom wall, especially in the entry region where organized thermal plumes are generated and the transition is triggered.

Table 2 shows the mesh resolution of the three meshes in the wall unit. The friction velocity u_τ is computed based on the wall shear stress at $x = 36$ cm, where [21] observed that the flow is fully developed. Grid #1 has a resolution similar to what is used for LES of a fully developed turbulent channel flow. Grid #2 has a finer resolution; the grid spacing in the x-direction is halved in the entire domain. The wall-normal (y) spacing is also smaller near the center of the channel. In Grid #3, the grid spacings in both x- and y-directions are reduced by half near the bottom wall. The grid spacing in the y-direction near the center of the channel is halved. The grid spacing at the cylinder's outer wall is the same for all cases. To perform the grid sensitivity analysis, conjugate heat transfer is not considered. Instead, the time-averaged temperature field from the experiment is used as the Dirichlet B.C. at the outer cylinder. The interpolated velocity profile from the experiment is used as the B.C. at $x = -3$ cm.

Fig. 11 shows contours of the instantaneous temperature using the three different grids in Table 2. Although Grid #1 would be sufficient for a fully turbulent channel flow, the results show that it is insufficient for the present case. The difference in results between Grids #2 and #3 is not as significant, but still visible. We observed that increased grid resolution results in a shorter bursting frequency of the initial thermal plumes and stronger mixing in the downstream region. The number of mesh points in Grid #3 is approximately 10 million.

Fig. 12 shows the averaged velocity profiles 5 cm upstream of the cylinder using the different grids. Compared to the experiment, the velocity profiles from the present study are distinctly asymmetric, but the asymmetry is reduced using finer meshes; however, the velocity profile from the experiment is not reproduced even when Grid #3 is used. The flow is asymmetric in the entry region because transition occurs only at the bottom wall. The symmetric profile from the experiment therefore implies that the flow is fully developed at 5 cm upstream of the cylinder. The RANS result of [21] shows a good agreement with the experiment because the x-velocity and kinetic energy profiles at $x = 36$ cm from the experiment were used as the B.C.s at the inlet (note that the cylinder is located at $x = 42.7$ cm).

Fig. 13 shows the averaged heat flux at the outer cylinder using the different grids. Interestingly, this quantity does not show strong dependency on the grid. This result implies that the averaged heat flux is insensitive to the upstream condition if a certain amount of mixing is achieved ahead of the cylinder. The results from the present study show a better agreement with the experimental data than the previous RANS result [21]. We believe that this is because the present study resolves the transition and the subsequent turbulence dynamics more accurately.

Fig. 14 shows the profiles of the square root of the kinetic energy defined as $k^{1/2} = \sqrt{(2\overline{u'^2} + \overline{v'^2})/2}$ at 5 cm upstream of the cylinder. The difference between results obtained on Grids #2 and #3 is not large, but both show large discrepancy with respect to the experiment. Fig. 15 shows contours of the instantaneous streamwise velocity and temperature using Grid #3. Large-scale thermal plumes are observed in the downstream region. These large-scale structures contribute significantly to

Table 2
Mesh spacings in wall units for grids in the heated cylinder case.

	Grid #1	Grid #2	Grid #3
$(\Delta x^+, \Delta y^+, \Delta z^+)$ at $\frac{y}{H} = 0$	(6.0, 0.24, 4.5)	(3.0, 0.24, 4.5)	(1.5, 0.12, 4.5)
$(\cdots)$ At $\frac{y}{H} = 0.5$	(6.0, 4.0, 4.5)	(3.0, 2.0, 4.5)	(3.0, 1.0, 4.5)
$(\cdots)$ At the outer cylinder	(0.12, 0.12, 4.5)	(0.12, 0.12, 4.5)	(0.12, 0.12, 4.5)

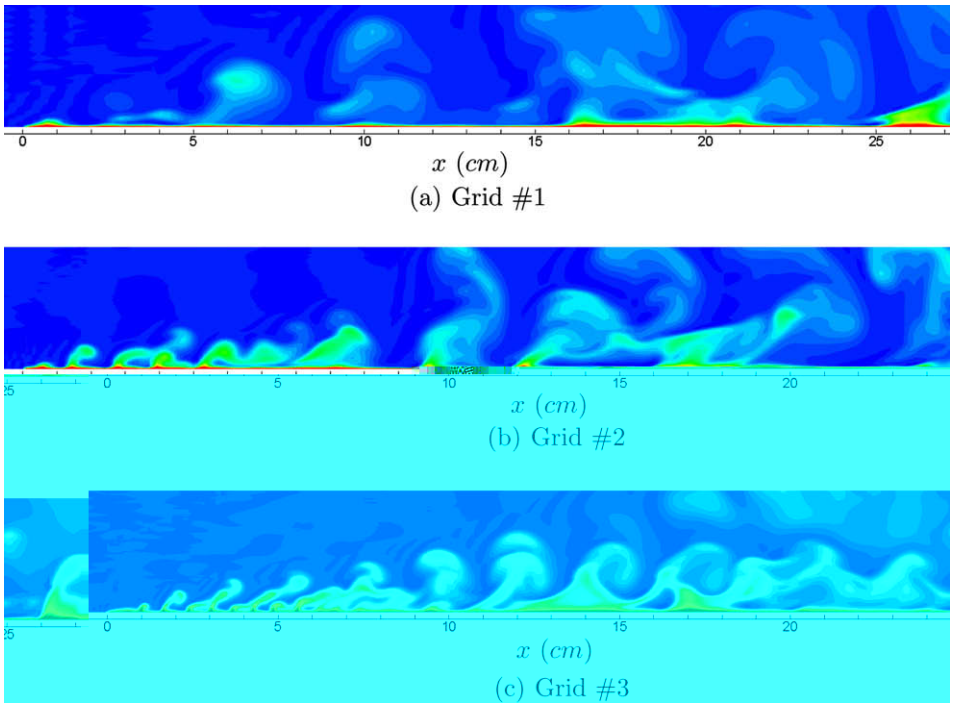

Fig. 11. Contours of the instantaneous temperature (T) using different grids in Table 2. 30 contour levels for T = 284–305 K.

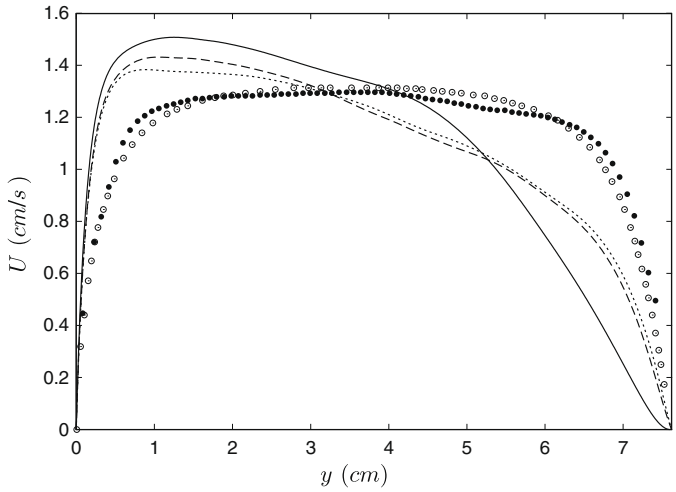

Fig. 12. Profiles of the averaged streamwise velocity at 5 cm upstream of the cylinder using different grids in Table 2: •, experiment [21]; ⊙, RANS [21]; —, Grid #1; - - - -, Grid #2; ····, Grid #3.

the kinetic energy. Assuming that the large-scale structures become weaker after the transition stage due to increased small-scale motions (as observed in [30]), the smaller kinetic energy profile from the experiment implies that the transition is completed earlier in the experiment compared to the simulations.

In summary, the strong dependency of the velocity and kinetic energy on the mesh resolution means that a very fine mesh is necessary for correctly predicting the transition in the entry region. Meanwhile, the averaged heat flux at the outer wall is shown to be much less sensitive to the mesh resolution. Although grid convergence is not strictly achieved, Grid #3 is chosen as the standard mesh in the present study. A possible explanation for the observed discrepancies with the experimental measurements is that the transition to turbulence in the present study is delayed with respect to the experiment.

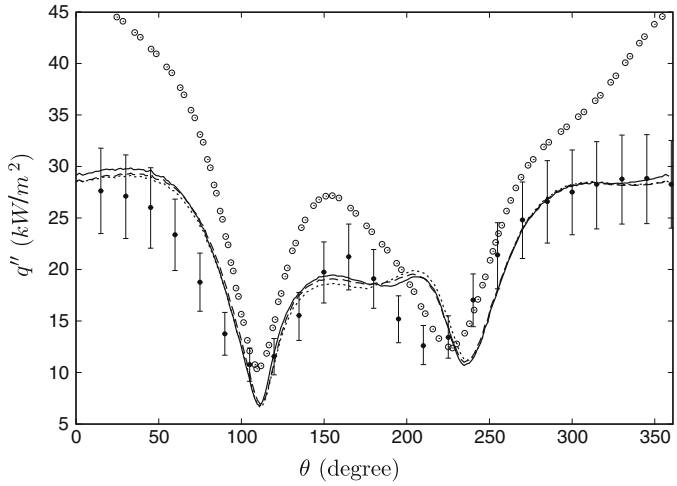

Fig. 13. The time-averaged heat flux at the outer cylinder using different grids in Table 2: •, experiment [21]; ⊙, RANS [21]; —, Grid #1; - - - -, Grid #2; ····, Grid #3. 0° and 90° correspond to the forward stagnation point and the top of the cylinder.

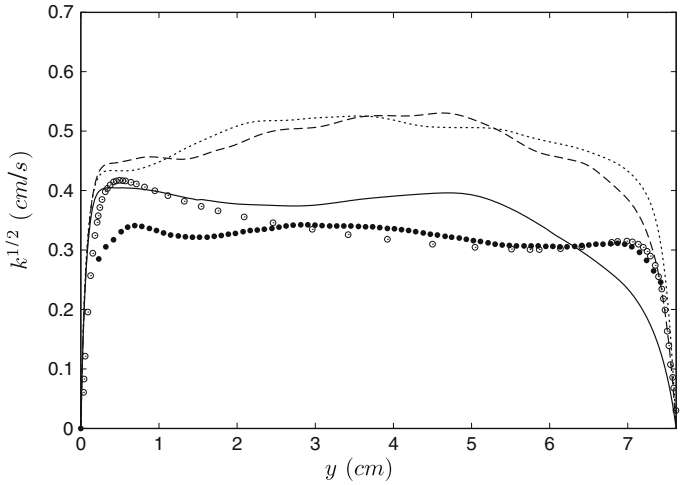

Fig. 14. Profiles of the square root of the kinetic energy at 5 cm upstream of the cylinder using different grids in Table 2: •, experiment [21]; ⊙, RANS [21]; —, Grid #1; - - - -, Grid #2; ····, Grid #3.

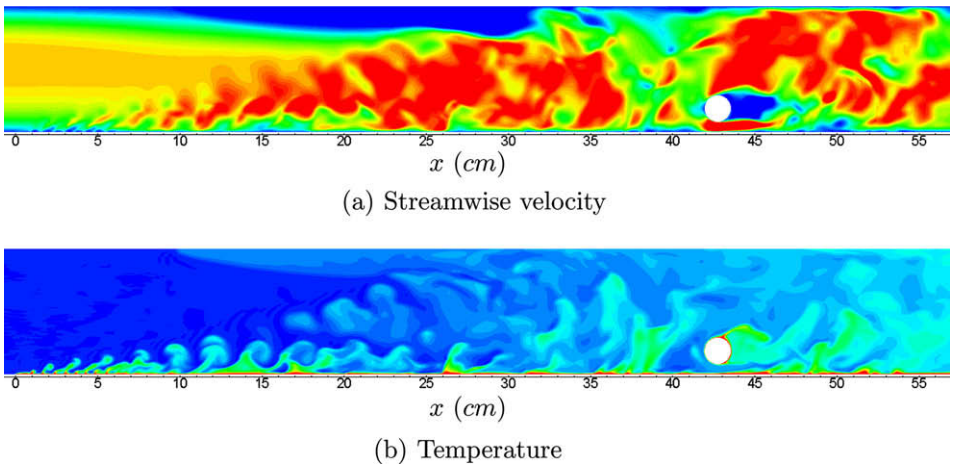

Fig. 15. Contours of the instantaneous streamwise velocity (u) and temperature (T) using Grid #3 in Table 2. 30 contour levels for u = 0.0–1.7 cm/s and 30 contour levels for T = 284–305 K.

4.4. Effect of inflow condition

Another important factor to consider in the transition to turbulence is the inlet velocity. The velocity B.C. described in the previous section is a steady profile obtained from the experiment. The presence of velocity fluctuations in the experiment is not documented, and therefore, here the effect of different inlet velocity profiles is investigated.

We considered three different velocity profiles. The first is interpolated from the experiment. The second is the uniform x-velocity profile ($=U_{in}$); we expect that this profile produces a high shear rate in the entry region, which may promote transition to turbulence. The third profile is a "recycled" velocity profile; in the RANS simulation of [21], the x-velocity and kinetic energy profiles at $x = 36$ cm from the experiment were used as the B.C.s at $x = 0$ cm. Using the same procedure employed in [21], the velocity profile at $x = 36$ cm is recycled to $x = -3$ cm. Note that the velocity is the only recycled variable; the temperature B.C. is not changed.

Figs. 16 and 17 show the averaged velocity at $x = 0$ and at 5 cm upstream of the cylinder, respectively, while Fig. 18 shows the kinetic energy profiles at 5 cm upstream of the cylinder using the different inlet velocity profiles. The case using the recycled B.C. shows the closest agreement to the measurements. The symmetry of the velocity is largely recovered. However, the kinetic energy profile is still over-predicted. An interesting finding is the poor agreement for the simulation using the uniform velocity profile.

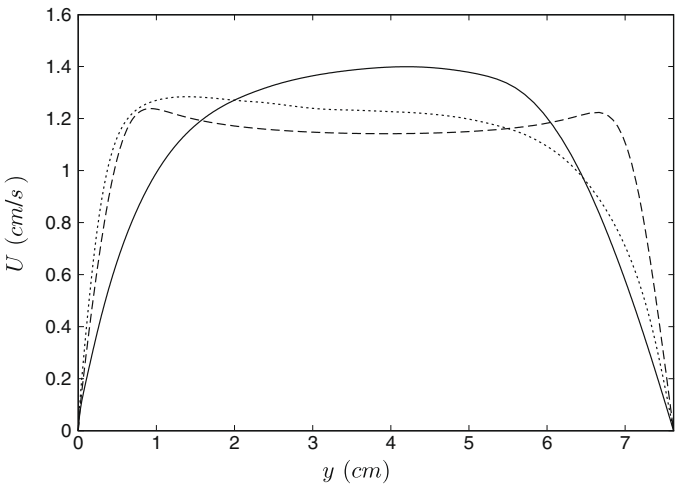

Fig. 16. Profiles of the averaged streamwise velocity at $x = 0$ using different inlet velocity profiles: —, interpolated from [21]; - - - -, uniform (U_{in}); ····, recycled from $x = 36$ cm.

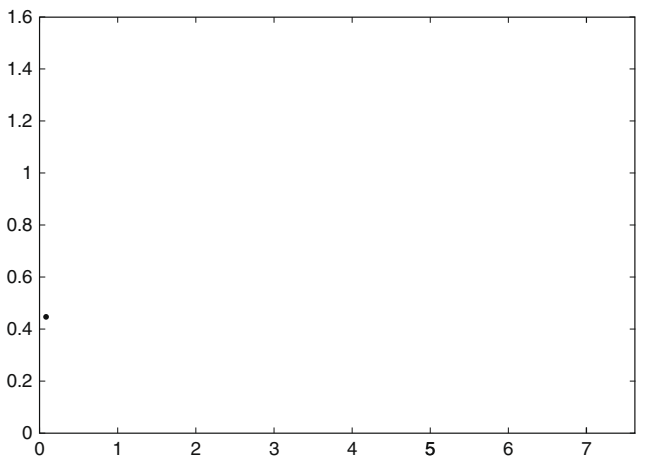

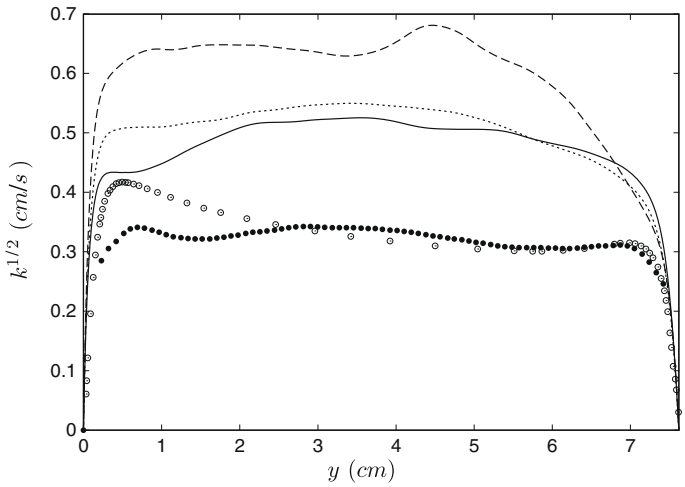

Fig. 18. Profiles of the square root of the kinetic energy at 5 cm upstream of the cylinder using different inlet velocity profiles: •, experiment [21]; ⊙, RANS [21]; —, interpolated from [21]; - - - -, uniform (U_{in}); ····, recycled from x = 36 cm.

Figs. 19 and 20 show contours of the instantaneous streamwise velocity and temperature. The instantaneous flow structures are qualitatively different with the three boundary conditions. The high shear rate from the uniform profile produces an instability that maintains organized laminar structures farther downstream than the other inflow conditions. Transition is therefore delayed, which results in a poor agreement with the measurements.

Fig. 21 shows the averaged heat flux at the outer cylinder. The heat flux values are similar for the cases using the interpolated and recycled velocity profiles. Based on the results, we can conclude that the averaged heat flux is not very sensitive to the inflow condition. With the uniform profile, the velocity field is laminar for a longer distance, which results in a relatively larger difference in the heat flux. The overall agreement is still good.

In conclusion, one finding in the present study is the difficulty in specifying the inflow to reproduce the experiment conditions. From the observation that transition occurs earlier in the experiment, the next step might be to introduce instability modes (for example uneven and unsteady thermal heating on the plate) to investigate the possible pathways to turbulence

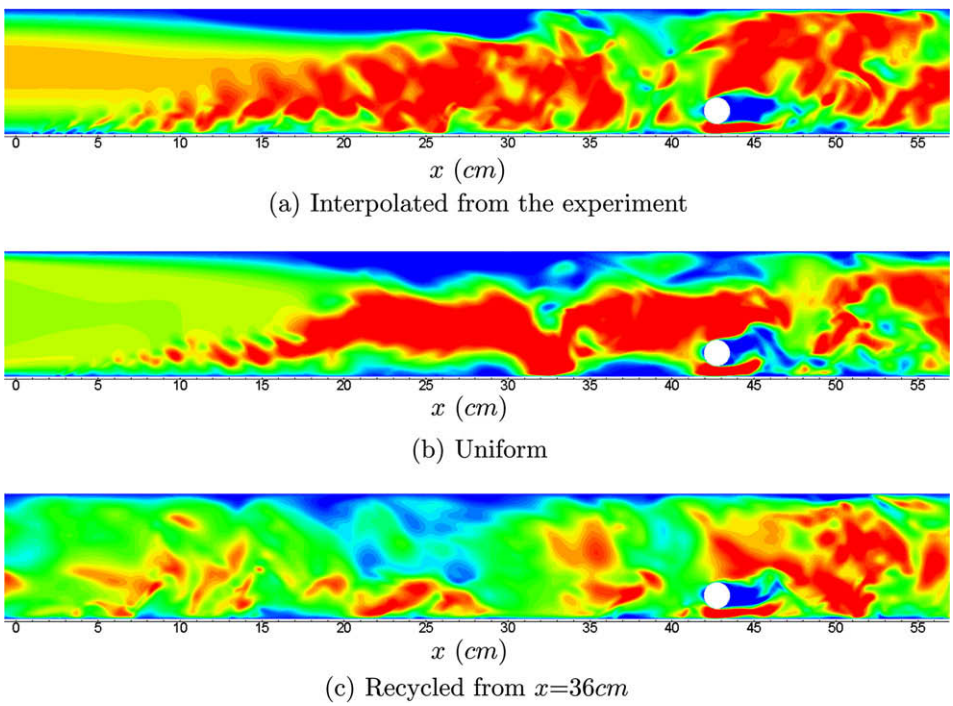

Fig. 19. Contours of the instantaneous streamwise velocity (u) using different inlet velocity profiles. 30 contour levels for u = 0.0–1.7 cm/s.

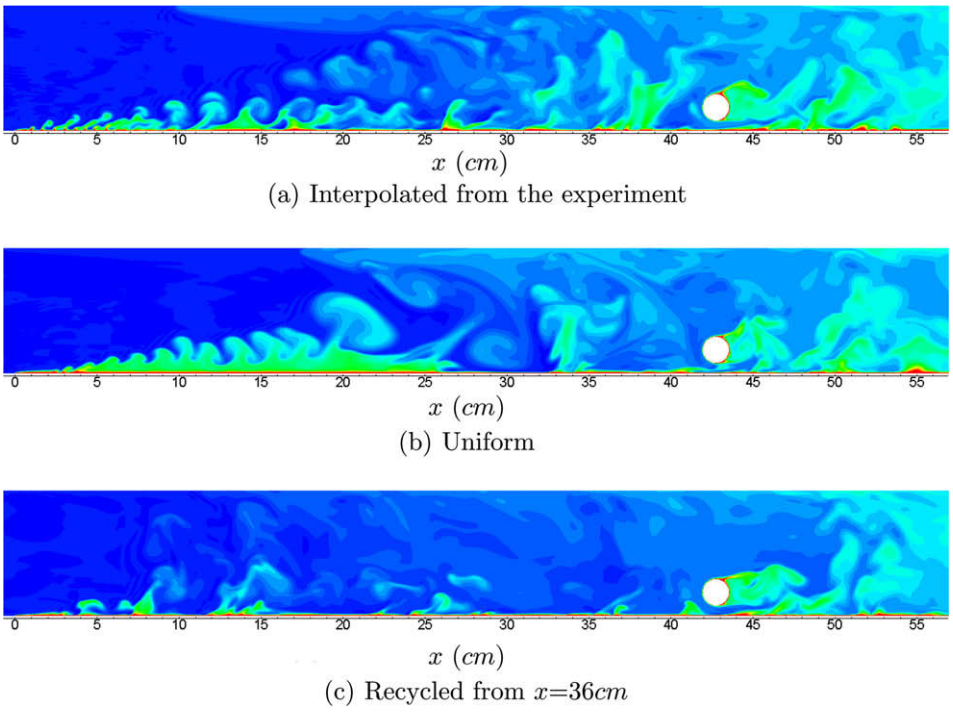

Fig. 20. Contours of the instantaneous temperature (T) using different inlet velocity profiles. 30 contour levels for T = 284–305 K.

breakdown. This analysis was clearly outside the scope of the present work and will be the subject of a future study. In spite of the uncertainty in the inflow, the averaged heat flux at the outer cylinder is not very sensitive to the inlet specifications.

4.5. Results with conjugate heat transfer

Fig. 22 shows the averaged heat flux at the outer cylinder for the cases with conjugate heat transfer. Two cases with different inlet velocity profiles – the interpolated profile from the experiment and the recycled profile – are compared to a case without conjugate heat transfer. Discrepancies are observed near the local maximum and minimum of the heat flux for the cases with and without conjugate heat transfer. Fig. 23 shows the RMS temperature at the outer cylinder; the regions of high RMS value coincide with the regions of relatively large differences between the two computational cases.

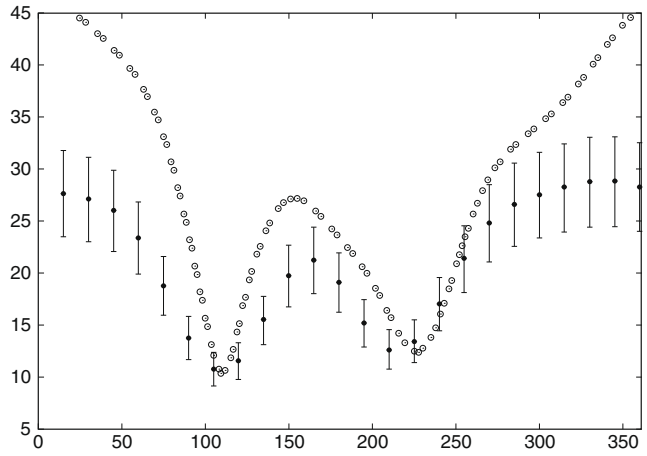

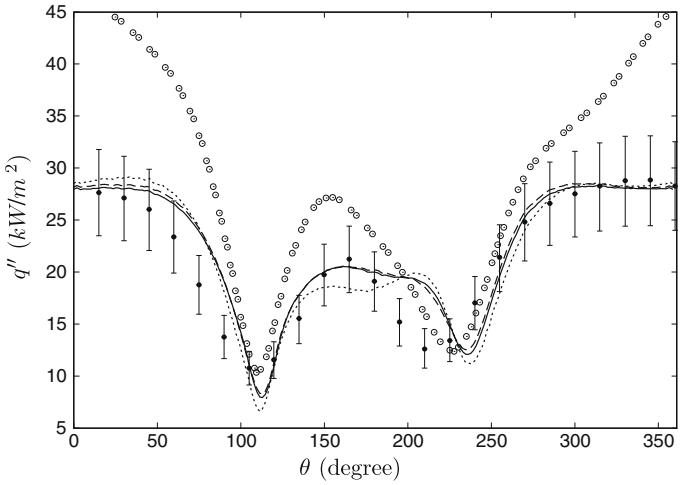

Fig. 22. The time-averaged heat flux at the outer cylinder: •, experiment [21]; ⊙, RANS [21]; —, with solid conduction and the interpolated inflow; - - - -, with solid conduction and the recycled inflow; ····, without solid condition and the interpolated inflow. 0° and 90° correspond to the forward stagnation point and the top of the cylinder.

Figs. 24 and 25 show contours of the instantaneous temperature. The temperature field inside the cylinder interacts with the vortex shedding behind the cylinder. Fig. 25(a) shows that initial thermal plumes are quasi-periodic in the spanwise direction, as well as in time. The initial thermal plumes are broken down by the subsequent downstream plumes and become turbulent.

Fig. 26 shows contours of the instantaneous heat flux at the outer cylinder and several radial locations inside the cylinder. Compared to the temperature (Fig. 24), the instantaneous heat flux visualizes the effect of flow structures on solid conduction more clearly; regions of low heat flux ($\theta \approx \pm 110$) at the outer cylinder (Fig. 26(a)) belong to separation points. These regions can be identified in all the other figures, which means that the effect of flow separation is present in the entire radial range of the solid. Near the upstream stagnation point ($\theta = 0$), the heat flux at the outer cylinder shows a large variation in the spanwise direction. Figs. 24 and 25 show that high temperature plumes intermittently impinge on the front side of the cylinder. This phenomena is closely related to the reduced local heat flux around $\theta = 0$.

4.6. Effects of the Boussinesq approximation and constant material properties

The results described in the previous sections are obtained using a variable density formulation of the Navier–Stokes equation Eqs. (1)–(3). In the present problem, the fluid is water, which has a small coefficient of thermal expansion ($=-(1/\rho)\partial\rho/\partial T$). The Boussinesq approximation with constant material properties Eqs. (7)–(9) is therefore the preferred

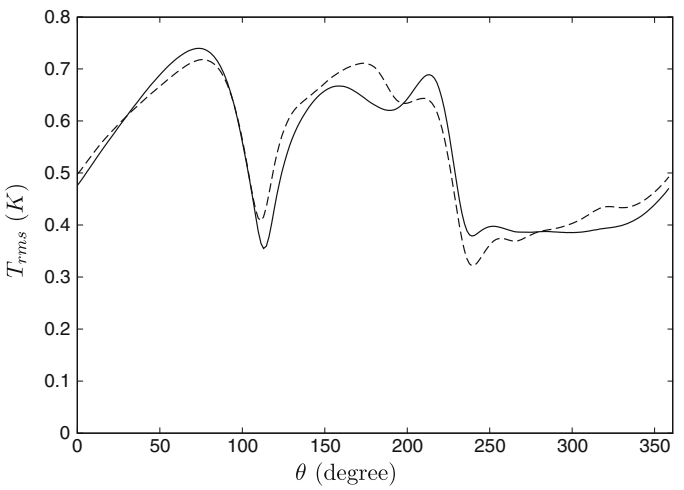

Fig. 23. RMS temperature at the outer cylinder for the cases with solid conduction: —, with the interpolated inflow; - - - -, with the recycled inflow. 0° and 90° correspond to the forward stagnation point and the top of the cylinder.

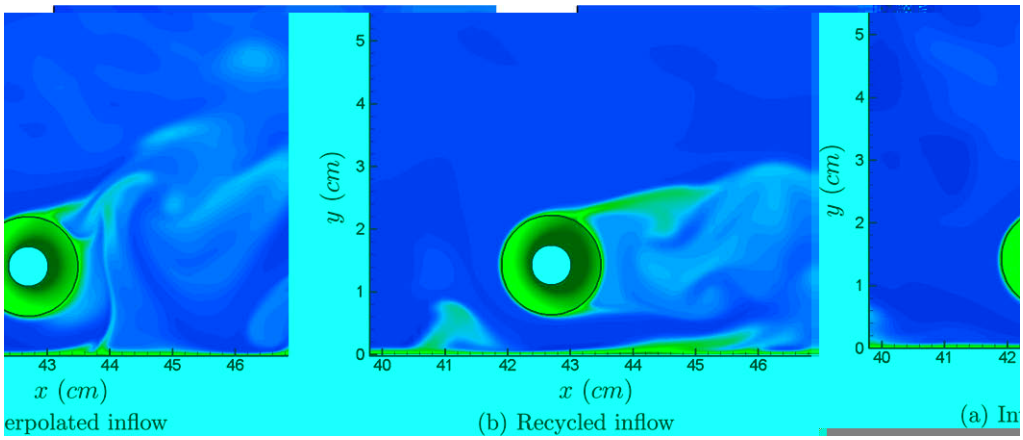

Fig. 24. Contours of the instantaneous temperature (T) with solid conduction (side view ($x - y$)). 60 contour levels for $T = 284$–320 K.

method for natural and mixed convection problems under these conditions. Fig. 27 shows the averaged velocity and kinetic energy profiles at 5 cm upstream of the cylinder obtained using the variable density formulation and the Boussinesq approximation. The difference between the two formulations does not appear to be significant. As previously mentioned, the averaged heat flux at the outer cylinder is relatively insensitive to the flow conditions.

A limitation of Eqs. (7)–(9) is the use of constant material properties. For example, in the present temperature range (from 284 to 318 K), the coefficient of thermal expansion β increases by 4 times. The kinematic viscosity ν also shows a large change – it decreases by half. As a consequence, the Grashof number ($Gr = g\beta\Delta TL^3/\nu^2$) increases by 16 times in the considered temperature range. Because of the strong sensitivity of the transitional regime to the fluid properties, the simulation results may vary significantly depending on the choice of reference temperature for the material properties. In order to verify the sensitivity to a specific choice of the reference temperature, simulations with Eqs. (7)–(9) are performed with three different reference temperatures: 284 K (T_{in}), 301 K (the film temperature = $(T_{in} + T_w)/2$), and 318 K(T_w). Fig. 28 shows contours of the instantaneous temperature. The three cases show very different flow structures and the results suggest that the variable density formulation in a transitional water flow with mixed convection is preferable, since it can remove the uncertainty in the definition of the (constant) material properties in the Boussinesq approximation. It is worth mentioning that with a proper

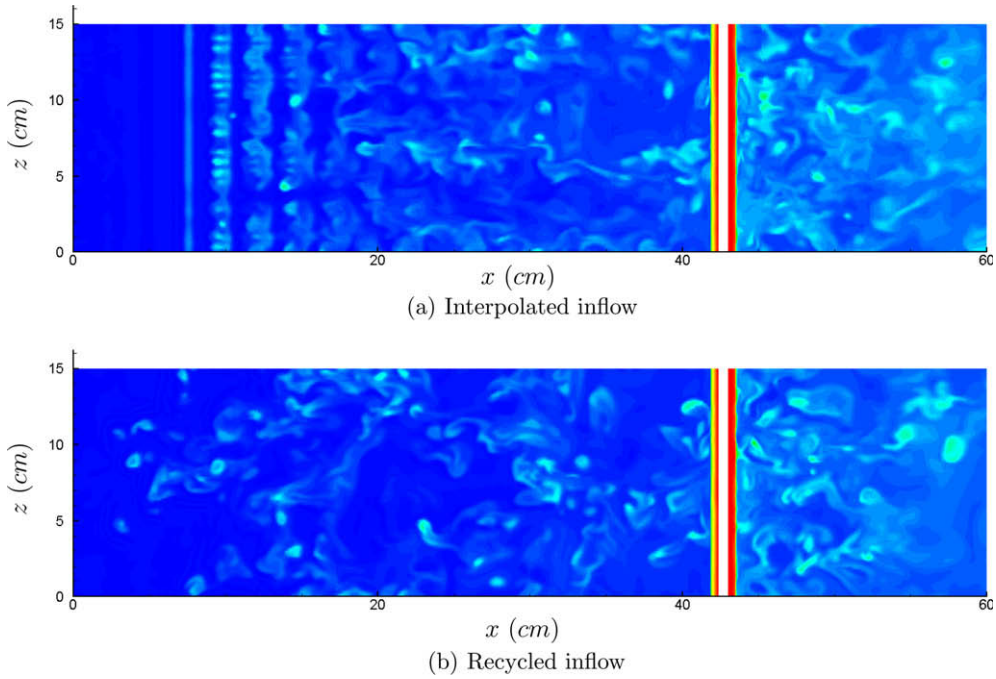

Fig. 25. Contours of the instantaneous temperature (T) with solid conduction (top view ($x - z$) at $y = 1.43$ cm). 60 contour levels for $T = 284$–318 K.

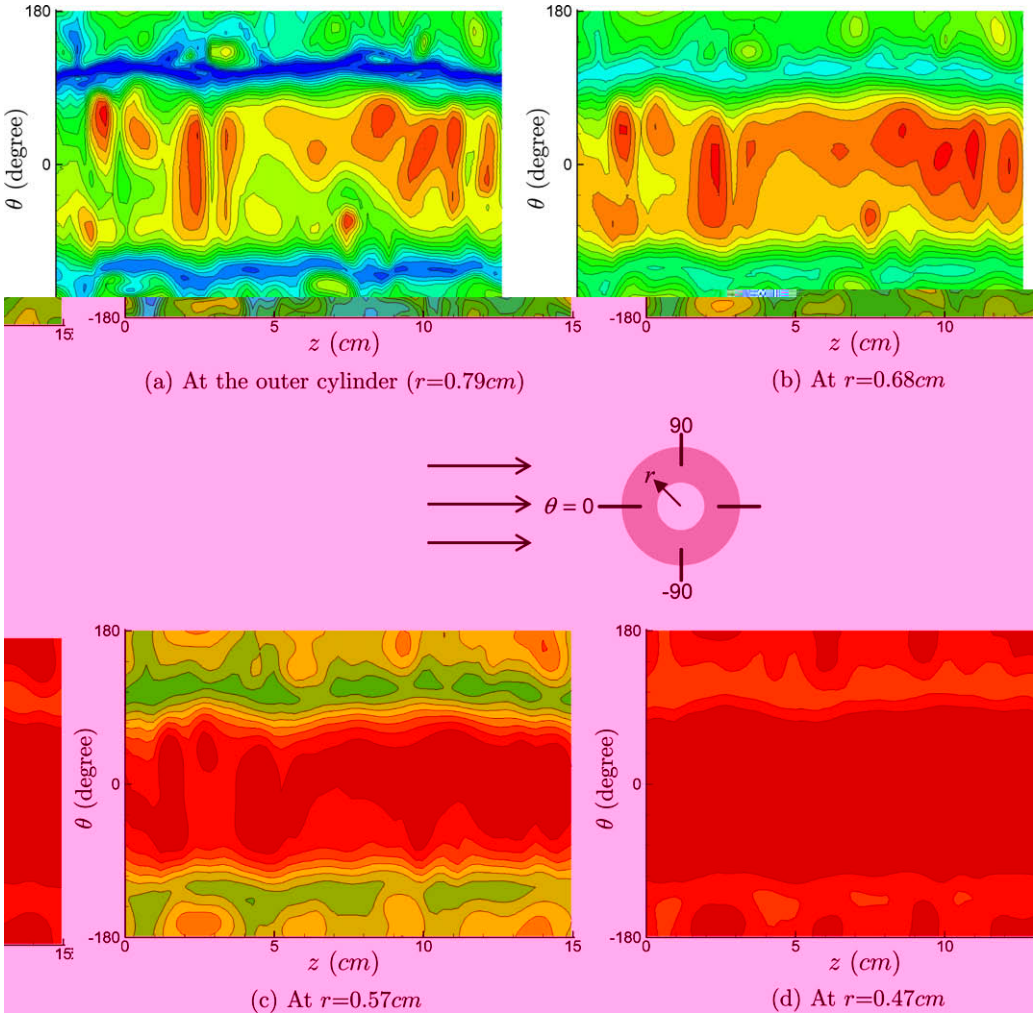

Fig. 26. Contours of the instantaneous heat flux ($q^{''}$) at several radial locations for the interpolated inflow case. 15 contour levels for $q^{''}$ = 8,940–35,760 kW/m^2. 0° and 90° correspond to the forward stagnation point and the top of the cylinder.

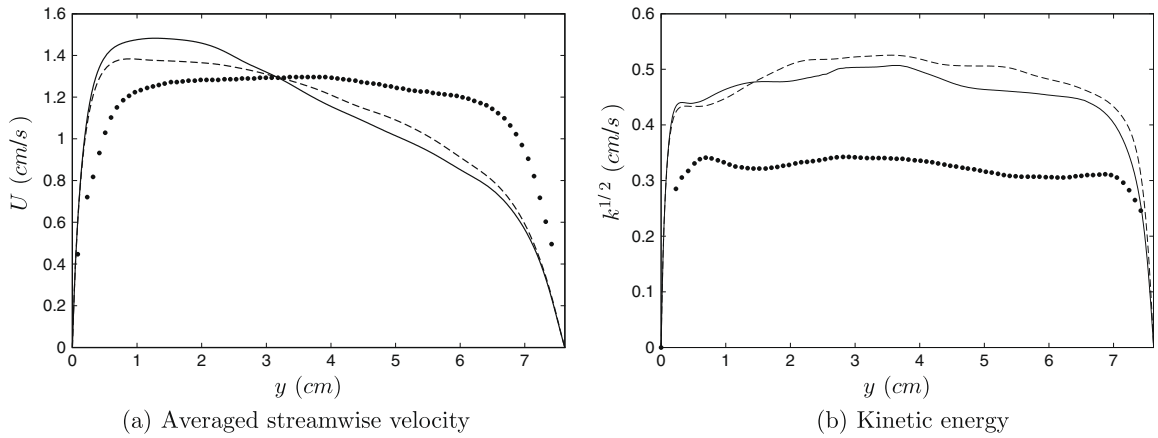

Fig. 27. Profiles of the averaged streamwise velocity and the square root of the kinetic energy at 5 cm upstream of the cylinder: •, experiment [21]; —, Boussinesq approximation with constant properties Eqs. (7)–(9); - - - -, variable density formulation Eqs. (1)–(3).

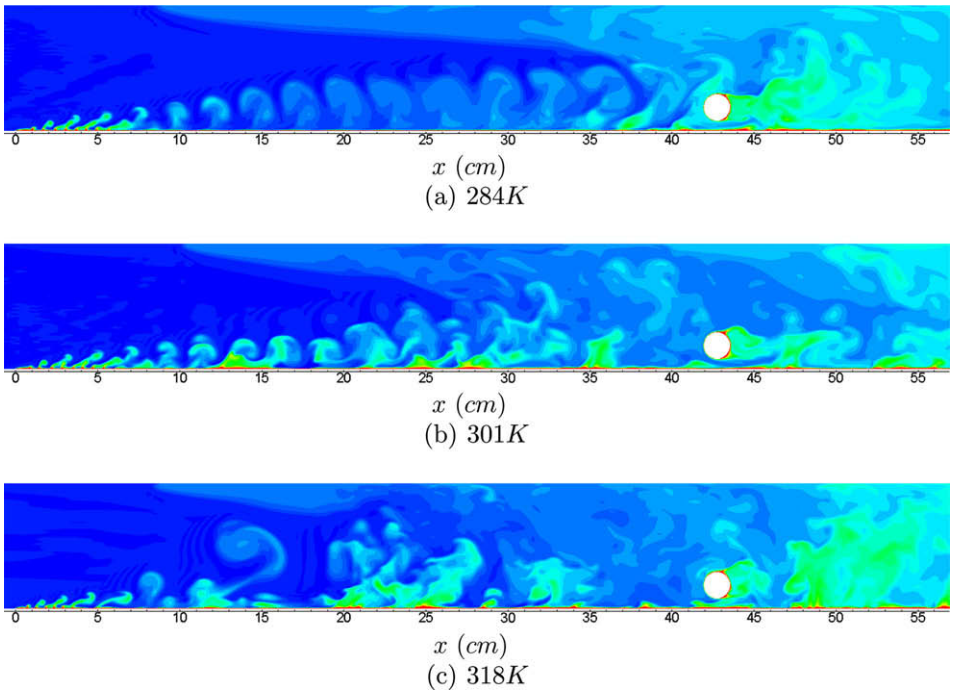

Fig. 28. Contours of the instantaneous temperature (T) using different reference temperatures. 30 contour levels for $T = 284$–305 K.

choice of (constant) β and ν (or the Grashof number), the computations performed using the Boussinesq approximation are comparable to the variable density predictions, as shown in Fig. 27.

5. Conclusions

The immersed boundary (IB) method has become popular for flow problems involving very complex geometries and moving bodies. In the present study, we utilized its capability of handling multi-material problems and assessed the IB method as an efficient tool for a turbulent conjugate heat transfer problem.

For multi-material problems, an approach based on immersed discontinuous grids has been developed. The fluid–solid interface consists of adjoining Cartesian faces from heterogeneous material zones. After projection of these faces onto the true material interface and the computation of the velocity reconstruction coefficients, the physical conditions for the material interface are satisfied by second-order interpolation. When applied to a canonical two-dimensional conjugate heat transfer problem, the approach shows first-order accuracy due to the one-sided finite-difference used to compute the heat flux.

The present approach was applied to the turbulent conjugate heat transfer problem of a heated cylinder in a channel with heating from below. In this application, an instability is triggered by thermal plumes originating from the heated bottom wall, and the flow transitions to turbulence. This process is observed to be very sensitive to the inflow conditions. As a result, a very fine mesh resolution is required in the upstream region of the cylinder. We used local mesh refinement to effectively reduce the number of computational mesh points in the presence of the large difference in length scales (i.e., small heated cylinder in a large channel). In contrast to the upstream flow field, the time-averaged heat flux at the cylinder outer wall is shown to be relatively insensitive to the mesh and inflow condition, and in general, the heat flux shows good agreement with the experiment. In contrast, the averaged velocity and kinetic energy profiles in the upstream of the cylinder show large deviations from the measurement. The inclusion of solid conduction in the heat transfer problem leads to better agreement with the experiment near the local maximum and minimum of the averaged heat flux. This has been explained with a large variation of the heat flux at the separation point. Although the fluid is water and has a small thermal expansion coefficient, simulations with the Boussinesq approximation with constant material properties show an uncertainty depending on the choice of reference temperature used to obtain the material properties, which requires a careful choice of physical parameters. Thus, the variable density formulation is preferred in the considered transitional flow with mixed convection.

Acknowledgment

Financial support from the Department of Energy under Advanced Simulation and Computing (DOE-ASC) program is gratefully acknowledged. We also thank the authors of Laskowski et al. [21] for their experimental data and suggestions.

References

[1] P.J. Atzberger, P.R. Kramer, C.S. Peskin, A stochastic immersed boundary method for fluid-structure dynamics at microscopic length scales, J. Comput. Phys. 224 (2007) 1255–1292.
[2] S.W. Churchill, Comprehensive theoretically based, correlating equations for free convection from isothermal spheres, Chem. Eng. Commun. 24 (1983) 339–352.
[3] P.A. Durbin, G. Iaccarino, An approach to local refinement of structured grids, J. Comput. Phys. 181 (2002) 639–653.
[4] E.A. Fadlun, R. Verzicco, P. Orlandi, J. Mohd-Yusof, Combined immersed-boundary finite-difference methods for three-dimensional complex flow simulations, J. Comput. Phys. 161 (2000) 35–60.
[5] L.J. Fauci, R. Dillon, Biofluidmechanics of reproduction, Annu. Rev. Fluid Mech. 38 (2006) 371–394.
[6] Y. Ge, L.-S. Fan, Three-dimensional direct numerical simulation for film-boiling contact of moving particle and liquid droplet, Phys. Fluids 18 (2006) 117104.
[7] R. Ghias, R. Mittal, H. Dong, A sharp interface immersed boundary method for compressible viscous flows, J. Comput. Phys. 225 (2007) 528–553.
[8] A. Gilmanov, F. Sotiropoulos, A hybrid Cartesian/immersed boundary method for simulating flows with 3D geometrically complex moving bodies, J. Comput. Phys. 207 (2005) 457–492.
[9] F. Ham, An efficient scheme for large eddy simulation of low-Ma combustion in complex configurations, Annual Research Briefs, Center for Turbulence Research, Stanford University, 2007, p. 41.
[10] F. Ham, K. Mattsson, G. Iaccarino, Accurate and stable finite volume operators for unstructured flow solvers, Annual Research Briefs, Center for Turbulence Research, Stanford University, 2006, p. 243.
[11] F.E. Ham, F.S. Lien, A.B. Strong, A Cartesian grid method with transient anisotropic adaptation, J. Comput. Phys. 179 (2002) 469–494.
[12] K.J. Hsieh, F.S. Lien, Conjugate turbulent forced convection in a channel with an array of ribs, Int. J. Numer. Methods Heat Fluid Flow 15 (5) (2005) 462–482.
[13] S. Huang, C.-H. Chun, A numerical study of turbulent flow and conjugate heat transfer in concentric annuli with moving inner rod, Int. J. Heat Mass Transfer 46 (2003) 3707–3716.
[14] G. Iaccarino, S. Moreau, Natural and forced conjugate heat transfer in complex geometries on Cartesian adapted grids, J. Fluids Eng. 128 (2006) 838–846.
[15] G. Iaccarino, R. Verzicco, Immersed boundary technique for turbulent flow simulations, Appl. Mech. Rev. 56 (3) (2003) 331–347.
[16] F.P. Incropera, D.P. De Witt, Fundamentals of Heat and Mass Transfer, third ed., John Wiley and Sons, 1990.
[17] H. Jia, G. Gogos, Laminar natural convection heat transfer from isothermal spheres, Int. J. Heat Mass Transfer 39 (1996) 1603–1615.
[18] S. Kang, An improved immersed boundary method for computation of turbulent flows with heat transfer. Ph.D. Thesis, Stanford University, 2008.
[19] W.M. Kays, M.E. Crawford, Convective Heat and Mass Transfer, third ed., McGraw-Hill, 1993.
[20] J. Kim, P. Moin, Application of a fractional-step method to incompressible Navier–Stokes equations, J. Comput. Phys. 59 (1985) 308–323.
[21] G.M. Laskowski, S.P. Kearney, G. Evans, R. Greif, Mixed convection heat transfer to and from a horizontal cylinder in cross-flow with heating from below, Int. J. Heat Fluid Flow 28 (2007) 454–468.
[22] Q. Liu, O.V. Vasilyev, A Brinkman penalization method for compressible flows in complex geometries, J. Comput. Phys. 227 (2007) 946–966.
[23] W.G. Mathers, A.J. Maddern Jr., E.L. Piret, Simultaneous heat and mass transfer in free convection, Ind. Eng. Chem. 49 (1957) 961–968.
[24] R. Mittal, G. Iaccarino, Immersed boundary methods, Annu. Rev. Fluid Mech. 37 (2005) 239–261.
[25] C. Pantano, R. Deiterding, D.J. Hill, D.I. Pullin, A low numerical dissipation patch-based adaptive mesh refinement method for large-eddy simulation of compressible flows, J. Comput. Phys. 221 (2007) 63–87.
[26] E. Papanicolaou, D. Giebert, R. Koch, A. Schulz, A conservation-based discretization approach for conjugate heat transfer calculations in hot-gas ducting turbomachinery components, Int. J. Heat Mass Transfer 44 (2001) 3413–3429.
[27] L.L. Pauley, P. Moin, W.C. Reynolds, The structure of two-dimensional separation, J. Fluid Mech. 220 (1990) 397–411.
[28] C.S. Peskin, The fluid dynamics of heart valves: experimental, theoretical, and computational methods, Annu. Rev. Fluid Mech. 14 (1982) 235–259.
[29] C.D. Pierce, Progress-variable approach for large-eddy simulation of turbulent combustion. Ph.D Thesis, Stanford University, 2001.
[30] M.M. Rai, P. Moin, Direct numerical simulation of transition and turbulence in a spatially evolving boundary layer, J. Comput. Phys. 109 (1993) 169–192.
[31] K. Shariff, R.D. Moser, Two-dimensional mesh embedding for B-spline methods, J. Comput. Phys. 145 (1998) 471–488.
[32] O.V. Smirnova, V.V. Kalaev, 3D unsteady numerical analysis of conjugate heat transport and turbulent/laminar flows in LEC growth of GaAs crystals, Int. J. Heat Mass Transfer 47 (2004) 363–371.
[33] P.K. Smolarkiewicz, R. Sharman, J. Weil, S.G. Perry, D. Heist, G. Bowker, Building resolving large-eddy simulations and comparison with wind tunnel experiments, J. Comput. Phys. 227 (2007) 633–653.
[34] J.C. Song, J. Ahn, J.S. Lee. Thermal resistance effect of solid wall on conjugate heat transfer in a ribbed channel, in: The Eighteenth International Symposium on Transport Phenomena, Daejeon, Korea, 2007.
[35] I. Tiselj, R. Bergant, B. Mavko, I. Bajsic, G. Hetsroni, DNS of turbulent heat transfer in channel flow with heat conduction in the solid wall, J. Heat Transfer-Trans. ASME 123 (2001) 849–857.
[36] M. Uhlmann, An immersed boundary method with direct forcing for the simulation of particulate flows, J. Comput. Phys. 209 (2005) 448–476.
[37] W.-M. Yan, Unsteady conjugated heat transfer in turbulent channel flows with convection from the ambient, Int. J. Heat Mass Transfer 38 (1995) 2101–2108.
[38] Z. Yu, X. Shao, A direct-forcing fictitious domain method for particulate flows, J. Comput. Phys. 227 (2007) 292–314.
[39] Z. Yu, X. Shao, A. Wachs, A fictitious domain method for particulate flows with heat transfer, J. Comput. Phys. 217 (2006) 424–452.
[40] H. Zhao, J.B. Freund, R.D. Moser, A fixed-mesh method for incompressible flow-structure systems with finite solid deformations, J. Comput. Phys. 227 (2008) 3114–3140.